Fast Huynen–Euler Decomposition and its Application in Disaster Monitoring

Liting Liang, *Student Member, IEEE*, Yunhua Zhang, *Member, IEEE*, and Dong Li, *Member, IEEE*

***Abstract*—Huynen–Euler (H–E) parameters proposed based on the diagonalization of the scattering matrix are of significant importance for single target information interpretation because of their explicit physical meanings. However, their application in target classification/recognition seems unsuccessful hitherto. Besides, the process of extracting the five H–E parameters by existing approaches, i.e., eigen-decomposition and unitary transformation, is a bit tedious and relatively time consuming, especially for large-sized polarimetric synthetic aperture radar (PolSAR) data. In this article, new H–E parameters are proposed to improve the performance of H–E decomposition in describing the scattering characteristics of the target. Furthermore, a fast decomposition approach is presented to derive the parameters directly and simultaneously with high computational efficiency. Another advantage of the fast H–E decomposition (FHED) is that, different from the original algorithm, which can only be applied to the single target, FHED is also effective for distributed targets, which expands the application range of the H–E decomposition. Experimental results on the temporal PolSAR data show that the changes in the disaster-affected area can be detected according to the changes in the newly proposed parameters, and the degree of change in the newly proposed skip angle has a linear relationship with the degree of urban damage. This indicates that FHED has a good prospect in disaster monitoring, especially for the estimation of building damage level (DL). It is also proved that the building DL mapped by the new skip angle and by the double-bounce scattering power, the most widely used parameter for such a situation, are highly consistent, while the former consumes much less time. Therefore, FHED can be applied to disaster monitoring and damage detection effectively, which is conducive to rescue operations by providing important information with a quick response.**

***Index Terms*—Building damage level (DL), computational efficiency, disaster monitoring, Huynen–Euler (H-E) parameters, polarimetric synthetic aperture radar (PolSAR).**

I. Introduction

POLARIMETRIC synthetic aperture radar (PolSAR) as a powerful remote sensing technology has provided human beings with more accurate results of target identification and terrain classification than traditional monopolarized SAR technology, since it is capable of acquiring the fully polarized information [1]. Polarimetric decomposition is of great significance for analyzing the polarimetric information of the target. As a forerunner researcher of the polarimetric decomposition theory, Huynen proposed a diagonalization form of Sinclair $[S]$ matrix with five Euler parameters as radar target magnitude m, target polarization orientation angle (POA) ψ, helicity angle τ, polarizability angle γ, and skip angle ν [2]. Huynen–Euler (H–E) parameters not only employ the polarimetric information completely, i.e., the number of H–E parameters and the degree of freedom (DoF) of scattering matrix are identical, but also all are related to specific physical characteristics of a pure target, i.e., m^2 is the maximum returned power reflecting target size, ψ denotes the rotated angle of the target about the line of sight of radar, τ determines target symmetry, ν has some relationship to depolarization owing to the number of bounces of the reflected signal, and γ is related to the target polarization sensitivity [2]. Table I lists some canonical scatterers and the values of their H–E parameters. It can be seen that the H–E parameter sets of different scattering mechanisms are different from each other, which indicates that theoretically, H–E decomposition can be used for target identification and classification. The proposal of H–E parameters has a far-reaching influence on the interpretation of target physical scattering characteristics, since almost all the algorithms later include at least one or more H–E parameters (though they may have different expressions from what

TABLE I
H–E Parameters of Different Canonical Scatterers

Canonical Scatterers	$[S]$	m	ψ	τ	γ	ν
sphere, plate, trihedral	$\begin{bmatrix}1 & 0\\ 0 & 1\end{bmatrix}$	1	0°	0°	45°	0°
dihedral	$\begin{bmatrix}1 & 0\\ 0 & -1\end{bmatrix}$	1	0°	0°	45°	45°
horizontal dipole	$\begin{bmatrix}1 & 0\\ 0 & 0\end{bmatrix}$	1	0°	0°	0°	0°
vertical dipole	$\begin{bmatrix}0 & 0\\ 0 & 1\end{bmatrix}$	1	90°	0°	0°	0°
right helix	$\frac{1}{2}\begin{bmatrix}1 & -j\\ -j & -1\end{bmatrix}$	1	0°	45°	0°	0°
left helix	$\frac{1}{2}\begin{bmatrix}1 & j\\ j & -1\end{bmatrix}$	1	0°	−45°	0°	0°

Manuscript received November 16, 2020; revised January 13, 2021 and March 14, 2021; accepted March 31, 2021. Date of publication April 5, 2021; date of current version April 28, 2021. This work was supported in part by the National Natural Science Foundation of China under Grants 41871274 and 61971402 and in part by the Strategic High-Tech Innovation Fund of Chinese Academy of Sciences under Grant CXJJ19B10. *(Corresponding authors: Liting Liang; Yunhua Zhang; Dong Li.)*

The authors are with the CAS Key Laboratory of Microwave Remote Sensing, National Space Science Center, Chinese Academy of Sciences, Beijing 100190, China, and also with the School of Electronic, Electrical, and Communication Engineering, University of Chinese Academy of Sciences, Beijing 100049, China (e-mail: liangliting16@mails.ucas.ac.cn; zhangyunhua@mirslab.cn; lidong@mirslab.cn).

Digital Object Identifier 10.1109/JSTARS.2021.3070897

Huynen proposed) [1], [3]–[9]. Nonetheless, the application of H–E decomposition in target classification/recognition seems unsuccessful hitherto, which is quite intriguing compared with the excellent performance of similar decomposition algorithm of Touzi [5], [6].

Besides, H–E parameters are generally derived by pseudo eigen-decomposition (ED) of scattering matrix or ED of the Graves matrix [1]. Even though Dallmann *et al.* proposed a new H–E decomposition technique on the basis of the submatrix of Kennaugh matrix recently, the calculation still depends on ED [10]. However, the computational cost is relatively large considering the high-resolution dataset with large size nowadays. On the other hand, Cameron *et al.* and Baird *et al.* derived H–E parameters by implementing a series of unitary transformations (UT) on $[S]$ [3], [4], [11]. This approach is inflexible, since it can only obtain one parameter a time by one UT operating, and the solving sequence of the parameters is fixed, which makes the calculation process not independent.

In this article, the unsatisfactory performance of the H–E decomposition is analyzed, according to which new parameters are proposed along with their solving approach, i.e., fast H–E decomposition (FHED). The newly proposed H–E parameters retain the explicit physical meanings while avoid the compressed range and ambiguous problem of the original. Besides, FHED indicates that neither ED nor the multi-step UT are necessary for calculation, since analytical expressions of the parameters can be derived directly from the parameterization form of $[S]$ based on Huynen parameters. Thus, H–E parameters can be computed directly and simultaneously with high efficiency.

With the increasingly frequent and intense occurrence of natural disasters in recent years, disaster monitoring and damage assessment as emerging applications of PolSAR data have attracted increasing attention, since using PolSAR data can remotely and swiftly extract information about large-scaled disaster affected areas [12]–[16]. By analyzing and comparing the scattering mechanisms before and after a natural disaster, the state of the related regions can be accurately recognized as intact, damaged, flooded, etc. Double-bounce scattering power extracted by model-based decomposition (MBD), which is usually considered as generating from building areas, is the most widely employed parameter [12]–[16]. Undoubtedly, timeliness is of great importance in responding to the disaster, and it is indicated that low-latency (at most 2–3 h) data are required to deliver the perishable information to be of use [17], [18]. Therefore, not only the rapid generation of the PolSAR data products is necessary, which has been realized by a recent achievement in NASA/JPL [17], but also the extraction of meaningful parameters requires high real-time performance. Note that the FHED extractions contain similar information as double-bounce scattering power, while the derivation of the former is more direct and prompt. Accordingly, it can be expected that FHED has a good application prospect in disaster monitoring, and the experimental results prove that it is indeed the case.

The remainder of this article is organized as follows. Section II recapitulates the theory of H–E decomposition, then new H–E parameters and the FHED are proposed in Section III. Experiments on the application of FHED in disaster monitoring and building damage assessment are discussed in Sections IV and V, along with the comparison of the computational efficiency of several relative approaches. Besides, the relationship between FHED and Touzi decomposition is also analyzed in Section V. Section VI concludes this article.

II. H-E Decomposition

A. Scattering Matrix and Huynen Parameters

The fully polarized information of a pure/single target can be modeled by the scattering matrix

$$[S] = \begin{bmatrix} S_{\mathrm{HH}} & S_{\mathrm{HV}} \\ S_{\mathrm{VH}} & S_{\mathrm{VV}} \end{bmatrix}. \tag{1}$$

Under the reciprocity condition, we have $S_{\mathrm{HV}} = S_{\mathrm{VH}}$ and the Pauli vector $\boldsymbol{k}$ is obtained as

$$\boldsymbol{k} = \frac{1}{\sqrt{2}} \begin{bmatrix} S_{\mathrm{HH}} + S_{\mathrm{VV}} \\ S_{\mathrm{HH}} - S_{\mathrm{VV}} \\ 2S_{\mathrm{HV}} \end{bmatrix}. \tag{2}$$

The target coherency matrix is then expressed as ([1] and [2])

$$\begin{aligned} [T] = \left\langle \boldsymbol{k} \cdot \boldsymbol{k}^{\dagger} \right\rangle &= \begin{bmatrix} T_{11} & T_{12} & T_{13} \\ T_{21} & T_{22} & T_{23} \\ T_{31} & T_{32} & T_{33} \end{bmatrix} \\ &= \begin{bmatrix} 2A_0 & C - jD & H + jG \\ C + jD & B_0 + B & E + jF \\ H - jG & E - jF & B_0 - B \end{bmatrix} \end{aligned} \tag{3}$$

where superscript † denotes the operation of complex conjugation and transposition, $\langle \cdot \rangle$ denotes ensemble average, T_{ij} is the (i, j) entry of $[T]$, and A_0, B_0, B, C, D, E, F, G, and H are the Huynen parameters [2]. Based on the phenomenological theory, the nine Huynen parameters contain physical information of the target, i.e., A_0 is considered as the total returned power from the regular and symmetric parts of the scatterer, $B_0 + B$ denotes the irregular depolarized power, whereas $B_0 - B$ represents the asymmetric depolarized power, C, D, E, F, and G are associated with the shape, local curvature, local twist (torsion), helicity, and local coupling (glue) of the scatterer, respectively, and H describes the target orientation [1], [2], [19].

B. H-E Decomposition

Huynen parameterized the scattering matrix $[S]$ with the five H–E parameters, as [2]

$$\begin{aligned} [S] = e^{j\xi} &\left([U_2(\psi)] [U_2(\tau)] [U_2(\nu)] \right)^* [S_D] \\ &\cdot \left([U_2(\psi)] [U_2(\tau)] [U_2(\nu)] \right)^{\dagger} \end{aligned} \tag{4}$$

where ξ is the absolute phase

$$[S_D] = m \begin{bmatrix} 1 & 0 \\ 0 & \tan^2 \gamma \end{bmatrix} \tag{5}$$

TABLE II
RANGES OF H–E PARAMETERS

Symbol	Quantity	Range Value
m	radar target magnitude	$[0, +\infty)$
ψ	POA	$[-90^\circ, 90^\circ]$
τ	helicity angle	$[-45^\circ, 45^\circ]$
γ	polarizability angle	$[0^\circ, 45^\circ]$
ν	skip angle	$[-45^\circ, 45^\circ]$
γ_n	new polarizability angle	$[0^\circ, 45^\circ]$
ν_n	new skip angle	$[0^\circ, 45^\circ]$

$$[U_2(\nu)] = \begin{bmatrix} e^{-j\nu} & 0 \\ 0 & e^{j\nu} \end{bmatrix} \tag{6}$$

$$[U_2(\tau)] = \begin{bmatrix} \cos\tau & j\sin\tau \\ j\sin\tau & \cos\tau \end{bmatrix} \tag{7}$$

$$[U_2(\psi)] = \begin{bmatrix} \cos\psi & -\sin\psi \\ \sin\psi & \cos\psi \end{bmatrix} \tag{8}$$

and $[U_2(\cdot)]$ is the special unitary SU(2) matrix. The explicit physical interpretation of the target by H–E decomposition is not only reflected in the extracted parameters, i.e., m, ψ, τ, γ, and ν have specific physical meanings as aforementioned, but also reflected in the UT, i.e., $[U_2(\nu)]$, $[U_2(\tau)]$, and $[U_2(\psi)]$ are generally considered to be related to the phase, symmetry, and orientation transformations of the target, respectively [1]–[4]. The range of each parameter is listed in Table II.

Although theoretically, H–E parameters are able to reflect the physical information of the target clearly, however, their application in target classification/recognition seems unsuccessful hitherto. By comparing with the widely used Touzi decomposition [5], which has the same definitions of ψ and τ as the H–E decomposition, it can be inferred that the problem lies in the basis-invariant parameters γ and ν, which are discussed as follows.

III. FAST H-E DECOMPOSITION

A. New Polarizability Angle γ_n

According to Huynen [2], γ is related to the target polarization sensitivity, which is reasonable since its parameterized form $\tan^2\gamma$ is just the diagonal element of matrix $[S_D]$. However, it is noted that the parameterization with the square of $\tan\gamma$ is unnecessary both physically and mathematically, since the only constraint of $[S_D]_{(2,2)}$ is

$$0 \le \frac{[S_D]_{(2,2)}}{m} \le 1 \tag{9}$$

as clearly specified by Huynen [2]. Actually, the utilization of $\tan^2\gamma$ leads to a distorted relation between the target polarization sensitivity and the extracted parameter γ. This is because the squaring operation will compress the value of γ in a smaller range due to the nonlinear projection, which will be discussed in detail later. Accordingly, $[S_D]$ is newly parameterized as

$$[S_D] = m \begin{bmatrix} 1 & 0 \\ 0 & \tan\gamma_n \end{bmatrix} \tag{10}$$

where $\gamma_n \in [0^\circ, 45^\circ]$.

TABLE III
DERIVED H–E PARAMETERS OF $[S_1]$ AND $[S_2]$ FORMULATED IN (12)

	ξ	m	γ	ν
$[S_1]$	90°	1	45°	-45°
$[S_2]$	-90°	1	45°	45°

B. New Skip Angle ν_n

As the most controversial parameter in H–E decomposition, skip angle ν was challenged for both its calculation and its physical significance. Even if these problems have been solved [20], [21], the ambiguity issue of ν still restricts its application.

For target with diagonal scattering matrix $[S]$, it can be modeled by H–E parameters as

$$[S] = me^{j\xi} \begin{bmatrix} e^{j2\nu} & 0 \\ 0 & \tan^2\gamma e^{-j2\nu} \end{bmatrix}. \tag{11}$$

Huynen believes skip angle ν, which ranges from -45° to 45°, has certain relationship to the bounces of the reflected signal [2], thus, it can be employed to differentiate sphere ($\nu = 0^\circ$) and dihedral target ($\nu = 45^\circ$). Nevertheless, problem arises when employing ν for dihedral target recognition. Consider two simple dihedral targets with scattering matrix $[S_1]$ and $[S_2]$

$$[S_1] = \begin{bmatrix} 1 & 0 \\ 0 & -1 \end{bmatrix}, \quad [S_2] = \begin{bmatrix} -1 & 0 \\ 0 & 1 \end{bmatrix}. \tag{12}$$

Table III shows their H–E parameters, which are derived according to (11). The different values of their skip angle, i.e., $\nu_1 = -45^\circ$ and $\nu_2 = 45^\circ$, mean that $[S_1]$ and $[S_2]$ are identified as two different kinds of target. However, since it can be derived that

$$[S_1] = e^{j180^\circ}[S_2] \tag{13}$$

the only difference between the two, actually, comes from the absolute phase term.

Since the paramount characteristic of double-bounce scattering is the opposite phase between the two copolar channels [1], it is reasonable to believe that the negative value of skip angle is ambiguous and the information of relative phase is sufficient. Accordingly, a correction is adopted for the skip angle, i.e., only the absolute value of ν is utilized for the description of target scattering characteristics, so as to avoid the aforementioned ambiguity. The new skip angle is expressed as

$$\nu_n = |\nu| \tag{14}$$

thus $\nu_n \in [0^\circ, 45^\circ]$.

C. FHED

Different from the two existing H–E decomposition methods, i.e., (pseudo) ED and UT, FHED decomposes the target directly using the analytical solution of H–E parameters. For convenience, we solve and represent the five on the basis of Huynen parameters, which are all real.

According to (2) and (4), the Pauli vector $\boldsymbol{k}$ can be expressed as

$$\boldsymbol{k} = \left([U_3(2\psi)]\,[U_3(2\tau)]\,[U_3(2\nu)]\right)^* \cdot \boldsymbol{k}_D \tag{15}$$

where

$$\boldsymbol{k}_D = \frac{m}{\sqrt{2}}\begin{bmatrix} 1+\tan\gamma_n \\ 1-\tan\gamma_n \\ 0 \end{bmatrix} \tag{16}$$

$$[U_3(2\nu)] = \begin{bmatrix} \cos 2\nu & -j\sin 2\nu & 0 \\ -j\sin 2\nu & \cos 2\nu & 0 \\ 0 & 0 & 1 \end{bmatrix} \tag{17}$$

$$[U_3(2\tau)] = \begin{bmatrix} \cos 2\tau & 0 & j\sin 2\tau \\ 0 & 1 & 0 \\ j\sin 2\tau & 0 & \cos 2\tau \end{bmatrix} \tag{18}$$

$$[U_3(2\psi)] = \begin{bmatrix} 1 & 0 & 0 \\ 0 & \cos 2\psi & -\sin 2\psi \\ 0 & \sin 2\psi & \cos 2\psi \end{bmatrix} \tag{19}$$

and $[U_3(\cdot)]$ is the special unitary SU(3) matrix. Thus, the coherency matrix of a single target can be parameterized as

$$\begin{aligned}[T] = {} & \left([U_3(2\psi)]\,[U_3(2\tau)]\,[U_3(2\nu)]\right)^* \cdot \boldsymbol{k}_D \cdot \boldsymbol{k}_D^{\dagger} \\ & \cdot \left([U_3(2\psi)]\,[U_3(2\tau)]\,[U_3(2\nu)]\right)^{\mathrm{T}}\end{aligned} \tag{20}$$

where superscript T denotes the operation of transposition. Accordingly, the Huynen parameters are obtained as

$$A_0 = \frac{m^2}{4}\left(1+\tan^2\gamma_n + 2\tan\gamma_n\cos 4\nu\right)\cos^2 2\tau \tag{21}$$

$$\begin{aligned} B_0 = {} & \frac{m^2}{4}\left(1+\tan^2\gamma_n\right)\left(1+\sin^2 2\tau\right) \\ & - \frac{m^2}{2}\tan\gamma_n\cos 4\nu\cos^2 2\tau \end{aligned} \tag{22}$$

$$\begin{aligned} B = {} & \frac{m^2}{4}\left(1+\tan^2\gamma_n\right)\cos^2 2\tau\cos 4\psi \\ & - \frac{m^2}{2}\tan\gamma_n\cos 4\nu\left(1+\sin^2 2\tau\right)\cos 4\psi \\ & - m^2\tan\gamma_n\sin 4\nu\sin 2\tau\sin 4\psi \end{aligned} \tag{23}$$

$$C = \frac{m^2}{2}\left(1-\tan^2\gamma_n\right)\cos 2\tau\cos 2\psi \tag{24}$$

$$\begin{aligned} D = {} & \frac{m^2}{4}\left(1+\tan^2\gamma_n + 2\tan\gamma_n\cos 4\nu\right)\sin 4\tau\sin 2\psi \\ & - m^2\tan\gamma_n\sin 4\nu\cos 2\tau\cos 2\psi \end{aligned} \tag{25}$$

$$\begin{aligned} E = {} & \frac{m^2}{4}\left(1+\tan^2\gamma_n\right)\cos^2 2\tau\sin 4\psi \\ & - \frac{m^2}{2}\tan\gamma_n\cos 4\nu\left(1+\sin^2 2\tau\right)\sin 4\psi \\ & + m^2\tan\gamma_n\sin 4\nu\sin 2\tau\cos 4\psi \end{aligned} \tag{26}$$

$$F = \frac{m^2}{2}\left(1-\tan^2\gamma_n\right)\sin 2\tau \tag{27}$$

$$\begin{aligned} G = {} & \frac{m^2}{4}\left(1+\tan^2\gamma_n + 2\tan\gamma_n\cos 4\nu\right)\sin 4\tau\cos 2\psi \\ & + m^2\tan\gamma_n\sin 4\nu\cos 2\tau\sin 2\psi \end{aligned} \tag{28}$$

$$H = \frac{m^2}{2}\left(1-\tan^2\gamma_n\right)\cos 2\tau\sin 2\psi. \tag{29}$$

It can be seen that different Huynen parameters reflect different characteristics of the target, and only five of the nine Huynen parameters are independent for a single target. According to (21)–(29), the analytical solutions of H–E parameters can be derived as

$$m = \sqrt{A_0 + B_0 + \sqrt{F^2+H^2+C^2}} \tag{30}$$

$$\psi = \frac{1}{2}\tan^{-1}\frac{H}{C} \tag{31}$$

$$\tau = \frac{1}{2}\tan^{-1}\frac{F}{\sqrt{H^2+C^2}} \tag{32}$$

$$\gamma_n = \tan^{-1}\sqrt{\frac{A_0+B_0-\sqrt{F^2+H^2+C^2}}{A_0+B_0+\sqrt{F^2+H^2+C^2}}} \tag{33}$$

$$\nu_n = \left|\frac{1}{4}\tan^{-1}\frac{(HG-CD)\sqrt{F^2+H^2+C^2}}{(A_0-B_0)(H^2+C^2)+2A_0F^2}\right|. \tag{34}$$

Consequently, the five can be solved directly and simultaneously with high efficiency. It is worth mentioning that in addition to simplicity, another key advantage for adopting Huynen parameters in H–E parameter representation is that they can be used for distributed targets, i.e., the application range of the original single target-only decomposition is expanded thus can deal with distributed targets if necessary, which will be further discussed and applied in the experimental part.

Note that $\tan\gamma_n$ in (33) is the square root of the term

$$\frac{A_0+B_0-\sqrt{F^2+H^2+C^2}}{A_0+B_0+\sqrt{F^2+H^2+C^2}} \tag{35}$$

while for the original parameterization form with $\tan^2\gamma$, the expression of γ is

$$\gamma = \tan^{-1}\sqrt[4]{\frac{A_0+B_0-\sqrt{F^2+H^2+C^2}}{A_0+B_0+\sqrt{F^2+H^2+C^2}}} \tag{36}$$

i.e., $\tan\gamma$ is the fourth root of (35). Due to the severe nonlinearity between (35) and γ, the latter will be compressed in a smaller range as aforementioned. This leads to a poor discrimination between targets, which will be substantiated in the following experiments.

(a) (b)

Fig. 1. Optical images of Ishinomaki, Miyagi acquired by ©Google Earth (a) before (taken on June 25, 2010) and (b) after (taken on April 6, 2011) the earthquake/tsunami, respectively. A to M are building areas with damage level (DL) 95%, 90%, 80%, 75%, 60%, 50%, 39%, 30%, 25%, 24%, 20%, 5%, and 0% (intact), respectively.

IV. Application of FHED in Disaster Monitoring

A. Disaster and Affected Area Description

The catastrophic magnitude 9.0 earthquake off the Pacific coast of Tohoku, which occurred on March 11, 2011, severely struck off the northeastern coast of Japan and triggered powerful tsunami waves that have reached heights of up to 40.1 m [16], [22]. It was the most powerful earthquake ever recorded in Japan, which has caused more than 15 899 deaths, 6157 injured, and 2529 people missing [12], [22]. In addition to the collapsing of hundreds of thousands of buildings, coastal areas suffered from floods caused by the earthquake-triggered tsunami. Fig. 1(a) and (b) shows optical images of Ishinomaki, Miyagi before and after the earthquake/tsunami, respectively. It can be seen that due to the tsunami, almost all buildings along the coast collapsed, and debris was washed away, while regions far from the coast were hardly affected.

B. Application of FHED on Distributed Targets

The temporal PolSAR data of the corresponding area were acquired by ALOS PALSAR on April 2, 2009, November 21, 2010, and April 8, 2011, respectively. To make the resolution in azimuth and range directions comparable, multilook processing was implemented on the original single look complex data in the form of $[T]$, with 12-look and 2-look in the azimuth and range directions, respectively [12]. Note that this averaged processing also incorporates the second-order statistical information of the target into the PolSAR data, which implies that the original data with single target scattering information is converted into the data with distributed target scattering information. Speckle and some random scattering components are also reduced since the essence of multilook processing is boxcar filtering [1].

As analyzed in Section III, FHED is an improved H–E decomposition with high computational efficiency, and they both are proposed based on the complete information extraction of the single target which has five DoFs. Although the multi-looked PolSAR data contains nine DoFs in its scattering information, here FHED is applied to it directly. Because the time spent for transforming a distributed target into several single targets is undesired for making a quick response to the disaster, especially when the data size is large. Therefore, in this article, the original and the improved H–E parameters of the distributed target both are solved by FHED. Undoubtedly, some polarimetric information of the target is lost during the decomposition, and it can be inferred that the degree of loss is related to the scattering randomness of the target. For instance, if the scattering characteristic of a target is stable and unchanged in a certain time and space, the effect of the multilooking is ignorable and it can still be considered as a single target, thus no information is lost by applying FHED. On the contrary, the scattering characteristics of an unstable target will be changed by multilooking, and according to the previous analysis, the random scattering component of the target is eliminated and the statistical information is introduced by the averaged processing. Therefore, it can be considered that the extracted H–E parameters by FHED compose a single scatterer, which reflects the most important scattering characteristics of the original distributed target. Similar to the widely applied polarimetric ED algorithm [23], which puts forward the concept of averaged scattering mechanism, the physical significance of H–E parameters extracted by FHED remains unchanged and can be interpreted as a description of the main polarimetric state of the target.

In order to quantitatively analyze the missing information of applying FHED to the distributed target, we in turn use the five derived H–E parameters, by (30)–(34), to reconstruct the nine Huynen parameters according to (21)–(29), and calculating their root mean square errors (RMSE), as

$$X_{\mathrm{RMSE}} = \sqrt{\frac{1}{M}\sum_{m=1}^{M}\left(X_{\mathrm{H\text{-}E}}^{(m)} - X^{(m)}\right)^2} \tag{37}$$

where m and M are the index of and the total number of the pixels in the whole image, respectively, X represents one of the nine original Huynen parameters, and $X_{\mathrm{H\text{–}E}}$ is the correspondingly reproduced Huynen parameter according to the extracted five H–E parameters. Table IV lists the calculated RMSE of the FHED-derived Huynen parameters. For comparison, the RMSE of Huynen parameters extracted from the eignvalue/eigenvector decomposition (EED) are also shown, where the EED-derived Huynen parameters are extracted from the coherency matrix produced by the principal eigenvector and the largest eigenvalue of the original coherency matrix, and it is a least-squares fit to the coherency matrix by a single scattering mechanism. Without loss of generality, the quantitative analysis here is based on the PolSAR data acquired in 2009. Table IV shows that, compared with EED, FHED has slightly worse performance in reproducing D, E, and G, similar in reproducing A_0, B_0, and B, but better in reproducing C, F, and H. This is because the reproduction of the Huynen parameters by FHED fully exploits the original Huynen parameters C, F, and H, as shown in (30)–(34), and

TABLE IV
COMPARISON OF FHED AND EED ON RMSE BETWEEN THE RETRIEVED AND ORIGINAL HUYNEN PARAMETERS

	A_0	B_0	B	C	D	E	F	G	H	A_0+B_0
FHED	0.1961	0.1961	0.2163	$3.9083e-16$	0.4073	0.1456	$1.5246e-16$	0.1267	$2.0924e-16$	$7.6817e-16$
EED	0.1111	0.1615	0.1236	0.1189	0.1552	0.0689	0.0163	0.0510	0.0333	0.0617

TABLE V
COEFFICIENT OF DETERMINATION OF THE FHED-DERIVED AND EED-DERIVED HUYNEN PARAMETERS

	A_0	B_0	B	C	D	E	F	G	H	A_0+B_0
FHED	0.9958	0.9844	0.9731	1	0.9798	0.9675	1	0.9824	1	1
EED	0.9987	0.9894	0.9912	0.9954	0.9971	0.9927	0.9956	0.9971	0.9931	0.9967

(21)–(29). Besides, RMSE of the combined parameter A_0+B_0 is also listed, since it is completely exploited in deriving the Huynen parameters, i.e., it exists in both (30) and (33). Actually, five DoFs are retained when reproducing Huynen parameters by the five H–E parameters, and according to (30)–(34), it can be inferred that A_0+B_0, C, F, and H compose four DoFs. Parameter representing the last DoF may have a complex expression because of the sophisticated expression of H–E parameter ν_n, which means it may be a combination of several Huynen parameters. It is unnecessary to find its explicit expression and knowing that it represents one DoF is enough for the present analysis. In general, the performance of FHED is consistent with the EED, which is also reliable in reproducing the Huynen parameters. This can be further verified by calculating the coefficient of determination R^2 of the fitting data, i.e.,

$$X_{R^2}=1-\frac{\sum_{m=1}^{M}\left(X_{\text{H-E}}^{(m)}-X^{(m)}\right)^2}{\sum_{m=1}^{M}\left(X^{(m)}-\bar{X}\right)^2} \tag{38}$$

where $\bar{X}$ is the averaged Huynen parameter of the whole scene. R^2 is a statistic that will give some information about the goodness of fit of a model. In regression, the R^2 coefficient of determination is a statistical measure of how well the regression predictions approximate the real data points. An R^2 of 1 indicates that the regression predictions perfectly fit the data. Table V compares the R^2 of FHED-derived Huynen parameters and EED-derived Huynen parameters, and both of them have high values. The result shown in Table V is in accordance with that in Table IV, i.e., FHED can perfectly reconstruct A_0+B_0, C, F, and H, while the performance is inferior on D, E, and G, and the accuracy of A_0, B_0, and B are in between. Nevertheless, all the R^2 of FHED-reproduced Huynen parameters are larger than 0.96, indicating a nice fitting of the original Huynen parameters. Therefore, in consideration of the nice reconstruction performance of FHED for target Huynen parameters, it is reasonable to applying it directly to the distributed targets. Consequently, the application scope of H–E decomposition is extended to the distributed target through FHED, and (30)–(34) are applied to the multilooked PolSAR data directly.

C. Overview of the Experimental Results

Figs. 2 and 3 show Pauli images and H–E parameters of the pre- and post-earthquake and tsunami PolSAR data, respectively, where in each figure, the three rows of images from top to bottom are the experimental results of PolSAR data obtained in 2009, 2010, and 2011, respectively. To analyze the performance of H–E parameters qualitatively, several sample areas of the ocean (circle I), built-up areas (squares II and III), and mountainous area (oval IV) are marked. Regions II and III were disaster-affected, while others were not. Furthermore, for quantitative analysis, areas with size 20×20 are extracted from different targets, i.e., the ocean (region I), buildings (region II), and mountainous area (region IV), and the histograms of their H–E parameters are plotted in Fig. 4 respectively. Each figure contains the results of the three datasets, and targets are distinguished by the red (buildings), green (mountains), and blue (ocean) colors. Here images shown in Figs. 2–4 are analyzed from two aspects. One is the performance of H–E parameters in describing the scattering characteristic of targets, i.e., attention would be paid on the images of the same date, and the other is the changes of H–E parameters pre- and post-disaster, i.e., results of different dates will be compared.

In general, the performance of H–E parameters in the first and the second rows of Figs. 2 and 3 are similar since the two data are both pre-disaster acquired during which the area almost has no change. It can be observed that H–E parameters have different characteristics for different kinds of targets. Since radar target magnitude m is related to the target scattering power [2], its range will be large when there is a coexistence of strong scattering targets and weak scattering targets. Hence, Fig. 2(b) depicts m in dB unit, i.e., $10\log_{10}m$, to avoid drowning details in the figures. m is strong in urban areas, weak in mountains, and much weaker in the ocean, rivers, and bare agriculture fields. As can be seen in Fig. 4(a), built-up areas and the ocean are clearly separated by -3 dB, and mountains are between the two. Orientation angle ψ of the urban areas is small and almost zero, since most of the buildings are aligned in the same direction with the flight direction of the PolSAR system [1]. ψ of mountainous areas fluctuates around zero, which may be the result of terrain slopes, and some ψ of the ocean is nearly -90° because of the Bragg scattering from the ocean surface [8]. Helicity angle

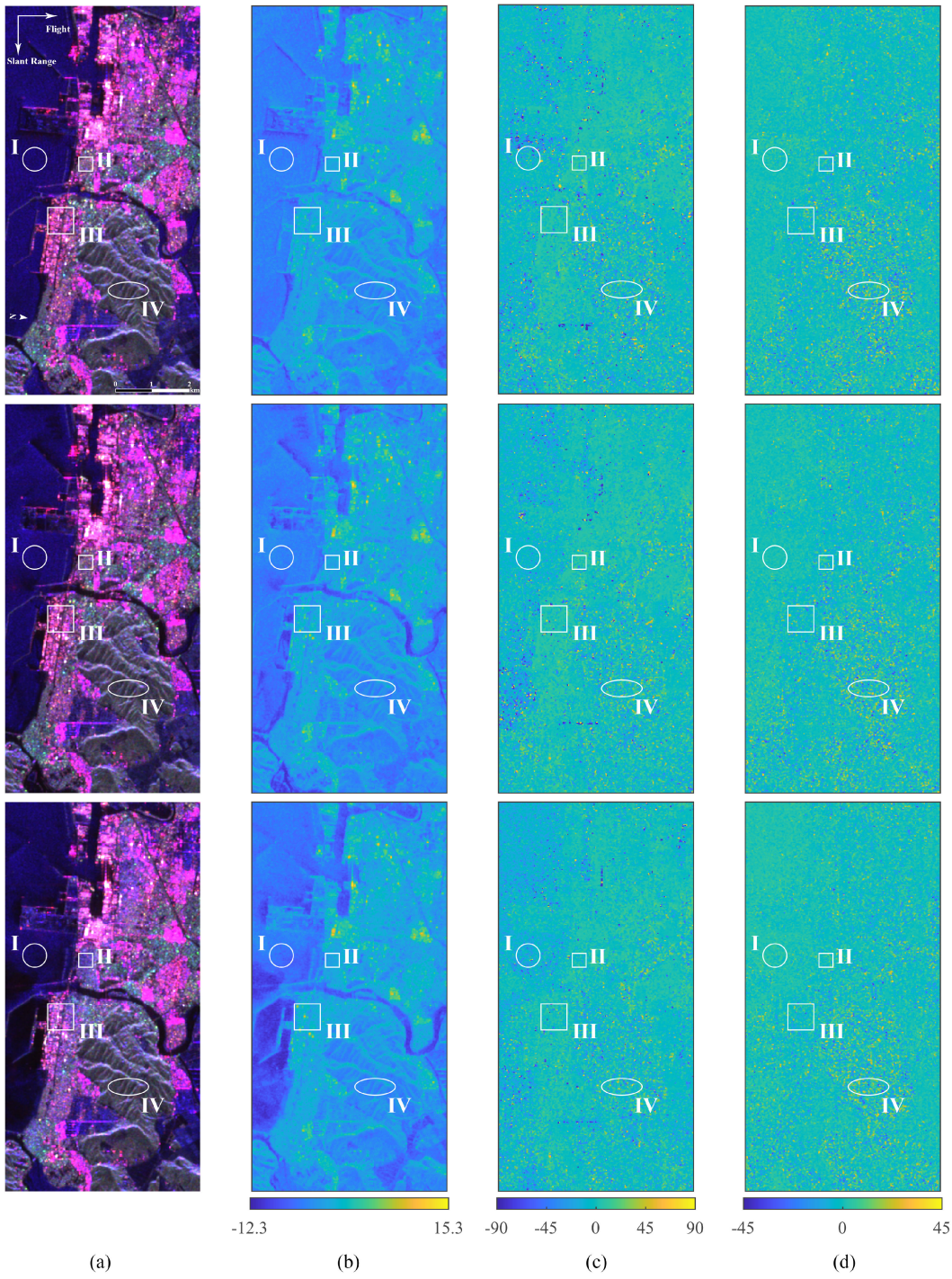

Fig. 2. Illustration of (a) Pauli images, (b) $10\log_{10}m$, (c) ψ, and (d) τ of PolSAR data acquired in (the first row) 2009, (the second row) 2010, and (the third row) 2011, respectively, where sample areas of ocean (circle I), built-up areas (squares II and III), and mountainous area (oval IV) are marked, and regions II and III were disaster-affected areas.

τ in the whole image fluctuates around zero in a small scope. It is commonly believed that τ has a strong relationship with target symmetry, i.e., it is large for manmade targets while small for natural targets [2]. However, the results in Fig. 4(c) show that τ should not be simply attributed as an index for building areas, since the distributions of τ in the urban area and the mountainous area seem the same, and there still needs more efforts to investigate its significance.

As analyzed in Section III-A, due to the range compression caused by solving the fourth root, γ in Fig. 3(a) is all large thus different targets can hardly be distinguished. It can be observed from Fig. 4(d) that all γ is huddled together in the

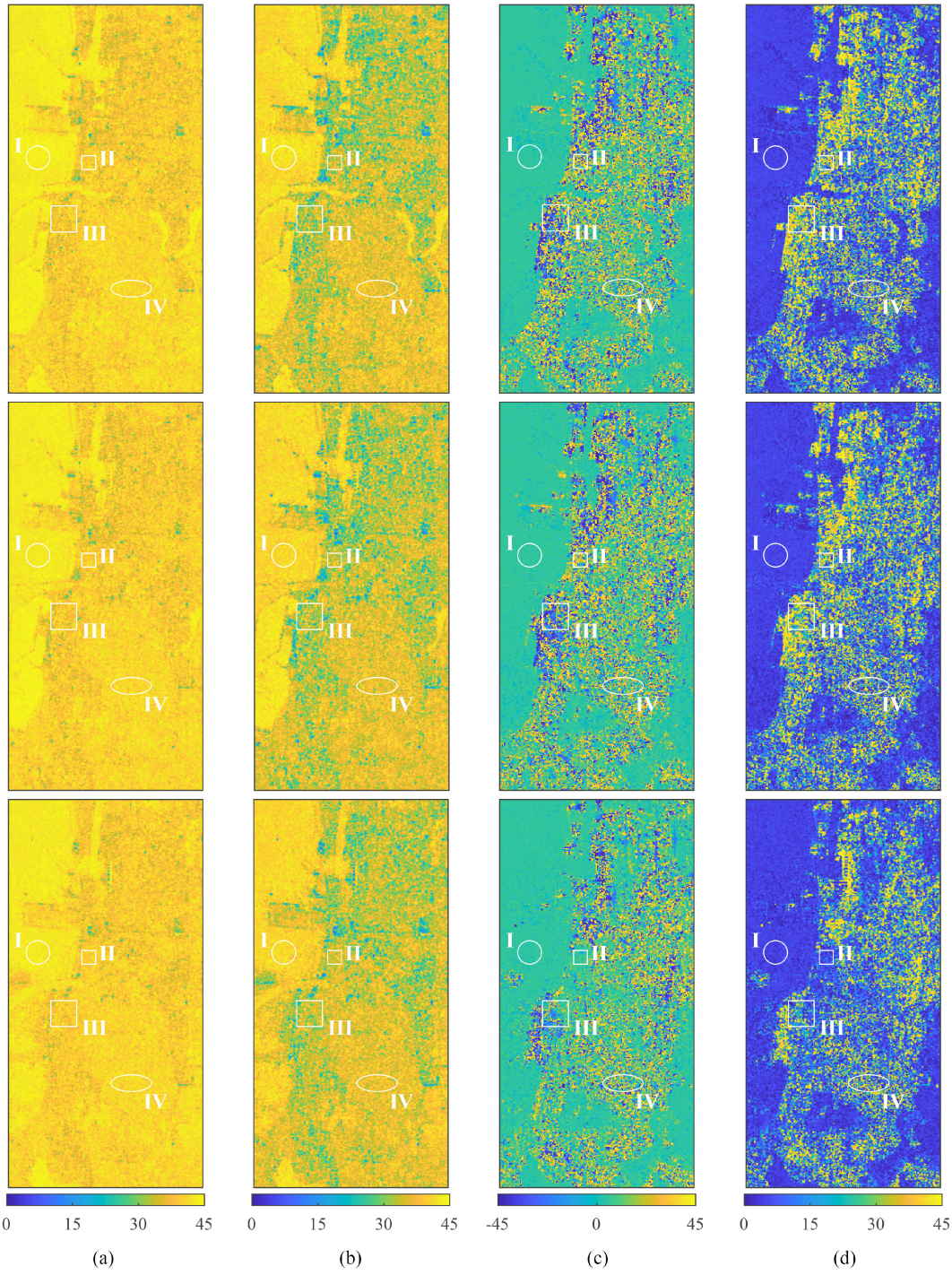

Fig. 3. Illustration of (a) γ, (b) γ_n, (c) ν, and (d) ν_n of PolSAR data acquired in (the first row) 2009, (the second row) 2010, and (the third row) 2011, respectively, where sample areas of ocean (circle I), built-up areas (squares II and III), and mountainous area (oval IV) are marked, and regions II and III were disaster-affected areas.

range of $[32^\circ, 45^\circ]$. While the newly proposed γ_n improves the performance of γ greatly, from which urban and mountainous areas can be told from the ocean areas clearly, i.e., the former range in $[30^\circ, 40^\circ]$ and the latter are greater than 40°. It is noted that rescaling γ directly, e.g., using parameter γ^2, also can improve the ability to distinguish targets to some extent. However, in consideration of the meaningful range of the angle and the representation simplicity, γ_n is adopted in FHED. Fig. 3(c) shows skip angle ν in $[-45^\circ, 45^\circ]$, which displays another scattering characteristic of the target. For ocean and crop areas that dominated by surface scattering, ν is around zero, while built-up and mountainous areas have higher absolute values of

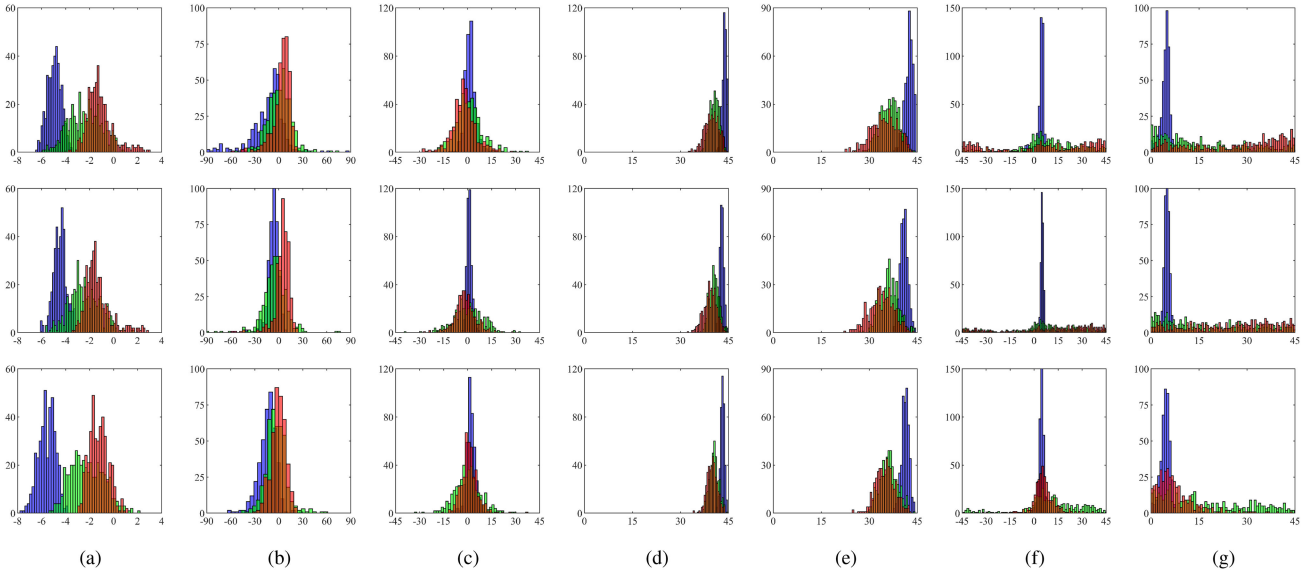

Fig. 4. Histograms of (a) $10\log_{10} m$, (b) ψ, (c) τ, (d) γ, (e) γ_n, (f) ν, and (g) ν_n on the temporal PolSAR data acquired in (the first row) 2009, (the second row) 2010, and (the thrid row) 2011, respectively, where the red, green, and blue bars represent urban areas, mountainous area, and the ocean, respectively.

ν. Besides, images of ν also reflect its ambiguous problem in dihedral target identification as discussed in Section III-B. For instance, both regions II and III, as marked by white squares in Fig. 3, are built-up areas, while their ν have opposite signs. Even if there is a possibility that the two parts are indeed different in some aspects, e.g., their materials, the different values of ν still induce an ambiguous classification result. ν_n avoids the problem and is effective for building recognition, as shown in Fig. 3(d), i.e., urban areas all have large ν_n values about 45°.

By comparing the pre- and post-disaster results of Figs. 2–4, it is noted that there are some clear changes in the coastal built-up areas. For instance, some reddish pixels along the coastal line are reduced as can be seen from the Pauli images in Fig. 2(a). In the images of m, some changes of area II can also be observed from Fig. 4(a), as some strong scattering points, larger than 1, are disappeared. No large changes happened on the values of ψ and τ that can be observed from Fig. 4(b) and (c), this is because the original urban area is dihedral scattering with zero orientation angle and zero helicity angle, and after the earthquake and the tsunami, which destroyed the buildings and washed away the debris, the dominant scattering mechanism is surface scattering, which has zero orientation angle and zero helicity angle also. This can also be proved by comparing the 2010 and 2011 results of Fig. 4(e), of which the γ_n of urban area moves toward the γ_n of the ocean slightly because of the changed scattering mechanism. In Fig. 4(g), ν_n of the built-up area after the disaster is significantly decreased, from original 45° to smaller than 15°. As afore-analyzed, this is also attributed to the changed scattering mechanism of the disaster-affected area.

Accordingly, the altered scattering mechanisms of the disaster-affected observations lead to the clear changes of γ_n and ν_n, which implies that the two proposed parameters can be employed for identifying disaster-affected areas, and even may be capable of assessing the extent of the building damage. Therefore, further quantitative analysis will be discussed later.

V. Urban DL Mapping

A. Building Damage Mapping With New H–E Parameters

The newly proposed basis-invariant parameters γ_n and ν_n and their application on DL mapping are further investigated because of the explicit physical significance related to the surface scattering and dihedral scattering, which are conducive in such situation. Building damage assessment is a crucial task in disaster monitoring, which can provide helpful instructions for rescue operation when a natural disaster occurs suddenly. To quantitatively apply the new H–E parameters to disaster monitoring, their relationships with the building DL [14], [24], [25] are investigated. As shown in Fig. 1, sample data of building areas with known ground truth DL are marked with red squares from A to M, of which the DL are 95%, 90%, 80%, 75%, 60%, 50%, 39%, 30%, 25%, 24%, 20%, 5%, and 0% (intact), respectively, and the sizes of these patches in the PolSAR data are 6×6 of patches A, B, C, and E, and 10×10 of the rest [14], [24], [25]. We define $\Delta\gamma_n$ and $\Delta\nu_n$, viz., the rate of the change of γ_n and ν_n, as indexes related to the degree of building damage, which are expressed as

$$\Delta\gamma_n = \frac{\gamma_{n(\text{pre})} - \gamma_{n(\text{post})}}{\gamma_{n(\text{pre})}} \tag{39}$$

$$\Delta\nu_n = \frac{\nu_{n(\text{pre})} - \nu_{n(\text{post})}}{\nu_{n(\text{pre})}} \tag{40}$$

where parameters with subscript (pre) and (post) are obtained from the data before and after the disaster, respectively. It can be inferred that for collapsed building areas, $\Delta\gamma_n$ is less than 0 and

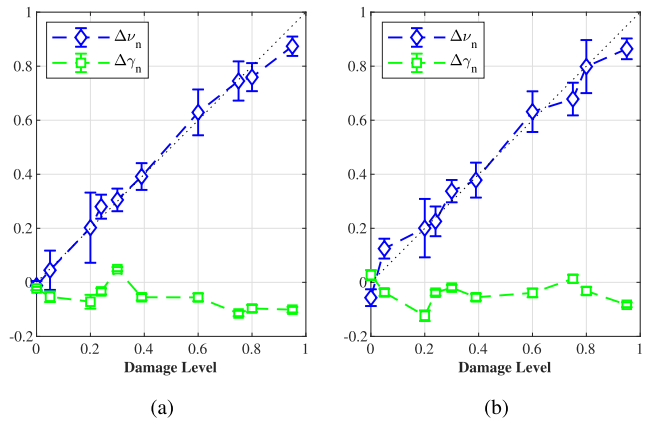

Fig. 5. Relationship between the ground truth DL and the damage indexes $\Delta\nu_n$ (the blue diamond) and $\Delta\gamma_n$ (the green square) for areas A (95%), C (80%), D (75%), E (60%), G (39%), H (30%), J (24%), K (20%), L (5%), and M (0%), where (a) and (b) are the results that based on the pre-disaster data acquired in 2009 and 2010, respectively.

$\Delta\nu_n$ is greater than 0. Besides, the more serious the damage is, the smaller the $\Delta\gamma_n$ and the larger the $\Delta\nu_n$ will be, theoretically.

As aforementioned, DL of building areas A to M are known, and areas A (95%), C (80%), D (75%), E (60%), G (39%), H (30%), J (24%), K (20%), L (5%), and M (0%) are employed to analyze the relationship among DL, $\Delta\gamma_n$, and $\Delta\nu_n$. Corresponding $\Delta\gamma_n$ and $\Delta\nu_n$ are calculated according to (39) and (40), and their relationships with the ground truth DL are plotted in Fig. 5. Note that since there are two pre-disaster PolSAR datasets, both of them are employed and the results are separately shown in Fig. 5(a) and (b). In general, $\Delta\gamma_n$ in Fig. 5(a) denoted by green squares satisfies the theoretical analysis, i.e., it decreases as the DL increases. However, it can hardly reflect any definite linear relationship since its variation range is too small compared with the fluctuations. Besides, the obvious abnormality at the H patch with DL=30% further reduces the feasibility of modeling between the two. The experimental result that $\Delta\gamma_n$ larger than 0 may be attributed to the influence of the vegetation in the area, i.e., before the disaster, the distributed vegetation in patch H contributes to the low averaged polarization sensitivity with a high value of $\gamma_{n(\text{pre})}$, while after the disaster, the vegetation is totally destroyed thus leads to the low value of $\gamma_{n(\text{post})}$. Even though the reduction of the buildings will increase the value of $\gamma_{n(\text{post})}$ theoretically, the effect of the 30% DL is too weak to balance the influence of the vanished vegetations. This can also be proved by $\Delta\gamma_n$ shown in Fig. 5(b), its value of the H patch is smaller than 0, since the data are acquired in the winter of 2010, which has less vegetations than spring (data of 2009 is acquired in April). On the other hand, $\Delta\gamma_n$ shown in Fig. 5(b) also fluctuates severely, of which a relation cannot be found with the ground truth DL. Essentially, the failure of $\Delta\gamma_n$ in describing building DL may be explained by the physical significance of γ_n. As the polarizability angle, γ_n reflects more about the target scattering difference between the two copolar channels instead of the scattering mechanism, while the former may be influenced by target material, shape, etc., which have little difference on built-up areas before and after the disaster. On the other hand,

TABLE VI
MODEL VERIFICATION ON AREAS B, F, AND I

Values	Area B	Area F	Area I
Ground Truth DL	0.9	0.5	0.25
Estimated DL (2009)	0.88	0.5247	0.2567
Estimated DL (2010)	0.8928	0.5175	0.2899

ν_n is the parameter clearly related to the scattering mechanism, which has a natural advantage in the estimation of building state. Unsurprisingly, $\Delta\nu_n$ in both Fig. 5(a) and (b) shows a nearly linear relation with DL, increasing with the increase of DL.

Consequently, a linear relationship can be established between $\Delta\nu_n$ and DL with the linear model

$$\text{DL} = k \cdot \Delta\nu_n + b \tag{41}$$

where k and b represent two constant parameters to be determined. Undoubtedly, for better establishing the relationship between a physical parameter and the urban DL, a fitting model can be obtained from the optimization point of view, as previous researchers have done [25]. However, the time consumption of model fitting is an undesirable cost when we aim to respond quickly to a sudden onset disaster, and the compatibility of the model for other PolSAR systems or other scenes also needs further investigation. Therefore, in this article, DL of the built-up area is estimated by the value of $\Delta\nu_n$ directly rather than model fitting, i.e., let $k = 1$ and $b = 0$, thus $\text{DL} = \Delta\nu_n$. Both Fig. 5(a) and (b) display a nice accordance between $\Delta\nu_n$ and the black dotted line, which is the angular bisector of the coordinate axes that through the origin, and the RMSE and the fitting R^2 between the two are 0.0279 and 0.9898 on 2009 data and 0.0382 and 0.9809 on 2010 data, respectively. To further verify the efficacy of the model, it is applied on areas B, F, and I for DL estimation. Table VI lists the results that are highly consistent with the true value, and RMSE for the comparison is 0.0188 on 2009 data and 0.0255 on 2010 data, showing that the model has a high degree of accuracy.

Accordingly, the map of building DL is acquired and shown in Fig. 6(a). Here, the pre-disaster data of 2009 is employed for mapping without loss of generality, since previous experiments have shown the similar results based on the data of 2009 and 2010. Although Fig. 6(a) clearly reflects the damaged condition of coastal areas, the mapped DL is somewhat noisy, especially for the ocean and mountainous areas. This is caused by the unstable scattering characteristics of these non-building areas, which may change with time and climate conditions. Actually, Chen *et al.* have discussed the influence of the temporal changes on the scattering mechanism in developing the technique of building DL estimation [14], and they limited the damage index Ratio_{Pd} in the range of $[0, 0.8]$ so as to avoid the interpretation ambiguity. Consequently, the DL Chen *et al.* estimated ranges from 20% to 100%. Similarly, we also take measures to reduce such random error, i.e., only the index values within $[0.2, 1]$ are utilized for urban DL inversion. Thus, the final expression of the

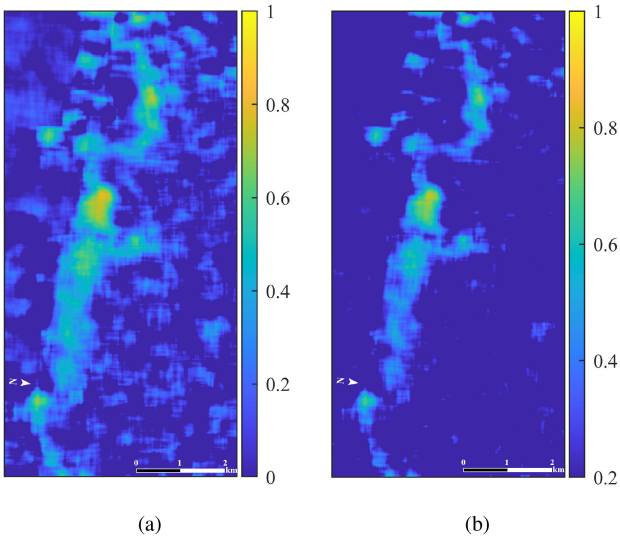

Fig. 6. Building DL map acquired by (a) $\Delta\nu_n$ and (b) the improved result of (a) which eliminates the influence of the non-building areas.

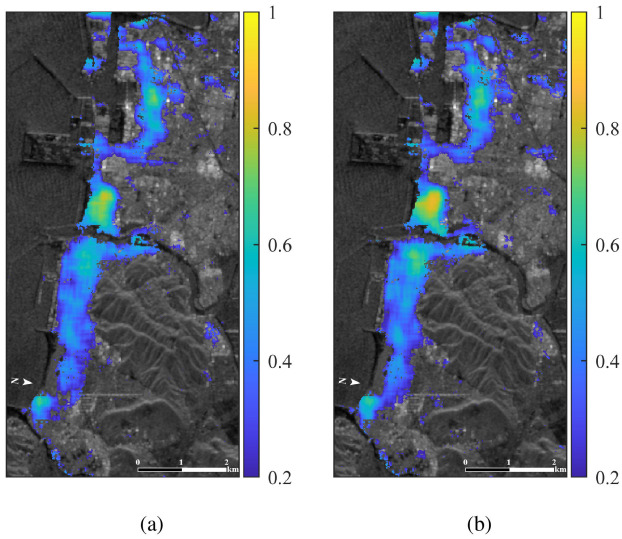

Fig. 8. Generated final urban DL map acquired by (a) $\Delta\nu_n$ based on (42) and (b) Ratio$_{Pd}$ proposed by Chen *et al.* [14]. The correlation coefficient between (a) and (b) is 0.9499.

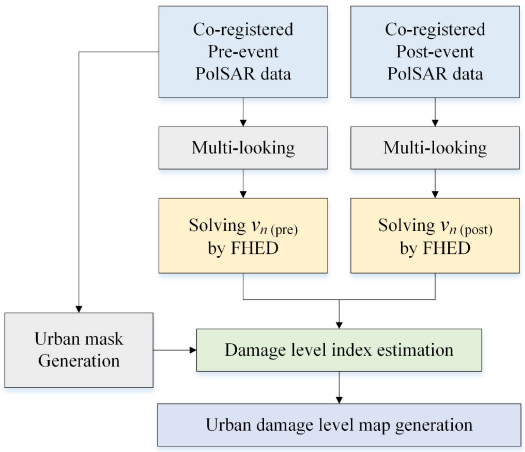

Fig. 7. Flowchart of urban damage mapping with the proposed method.

estimated DL is

$$\mathrm{DL} = \begin{cases} 1, & \Delta\nu_n > 1 \\ \Delta\nu_n, & 0.2 \le \Delta\nu_n \le 1. \\ 0, & \text{others} \end{cases} \tag{42}$$

As shown in Fig. 6(b), the improved result given by (42) displays a clear map of the building DL of the scene.

The flowchart of the urban DL mapping is shown in Fig. 7, where the urban mask is generated by the same method as in [14] and [24]. With the flowchart and the relationship expressed by (42), the final DL mapping result of the scene is shown in Fig. 8(a), which is superimposed on the SPAN image, and the damage map acquired by MBD proposed by Chen *et al.* is shown in Fig. 8(b) [14]. The two maps show similar estimations on the whole, while the damage extent estimated by $\Delta\nu_n$ seems lower than that estimated by Ratio$_{Pd}$ at the most severely damaged areas, i.e., region II marked by the white square in Fig. 2(a).

In fact, the same phenomenon also exists in the quantitative estimation in Fig. 5 and Table VI, i.e., DL estimation results of region A, B, and C are all underestimated slightly. Mathematically, this phenomenon is caused by a higher $\nu_{n(\mathrm{post})}$ value or a lower $\nu_{n(\mathrm{pre})}$ value than they should be, and since $\nu_{n(\mathrm{post})}$ in region II are all around zero as clearly displayed in Fig. 3(d), the problem lies in the low $\nu_{n(\mathrm{pre})}$ values. It can be seen that there are some distributed points with fairly small $\nu_{n(\mathrm{pre})}$ values in region II, which show a similar characteristic of non-building areas. This may be attributed to the scattering of streets and the complex building conditions of the area (houses are densely packed), and the small $\nu_{n(\mathrm{pre})}$ value is averaged through the moving window for obtaining the final DL map, which greatly decreases the averaged $\nu_{n(\mathrm{pre})}$ value, thus the DL are underestimated and smaller than the true values at severely damaged areas. The adopted size of the moving window is 15×15, a result of a theoretical determination [14], [24]. However, it is worth mentioning that the quantitative comparison in Fig. 5 and Table VI on the sample data from A to M displays that the error of the estimation is small, and the overall nice accordance between the truth and the estimated substantiates the efficacy of the proposed parameter. Besides, the estimations shown in Fig. 8(a) and (b) are highly correlated, i.e., their correlation coefficient is 0.9499, which means that a more accurate result can be obtained by a more proper fitting-model for $\Delta\nu_n$ and this may be further investigated in the future work. On the other hand, the good performance of $\Delta\nu_n$ in describing the change of building scattering characteristics before and after a disaster has its huge advantage in consideration of its high computational efficiency, which is further investigated in the next section.

B. Computational Efficiency of FHED

As aforementioned, one of the advantages of applying FHED to disaster monitoring is its high computational efficiency.

TABLE VII
TIME CONSUMPTION OF DIFFERENT METHODS ON DISASTER DATA

Data Size	Time Consumption*			
	FHED	UT	ED	MBD
1248×18432	0.2458	2.2704	209.0866	4.9178

1) *Unit: second (s).

Actually, the efficiency of the algorithm is not only superior to the traditional H–E decomposition methods, but also outperforms the widely used algorithm MBD, which leads to its undoubted superiority in rapid response to a sudden onset disaster. The time consumption for extracting DL-related parameters, i.e, ν_n of the three H–E decomposition approaches and Pd of MBD, are compared on the disaster PolSAR data, as shown in Table VII, which are processed within a computer hardware environment of Intel (R) Core (TM) i7-9700 CPU, 3.00 GHz CPU clock, 16.00 GB of memory, as well as a software environment of MATLAB R2019b. To reduce the random error, all the computations are conducted five times and the data recorded are averaged. Unsurprisingly, FHED with analytical solutions has the highest computational efficiency, while ED is the most time consuming, and UT and MBD are somewhere in between. FHED, UT, and MBD all take much less time than ED, which is unbearable for the large-sized PolSAR data. However, compared with the proposed, UT and MBD are still time consuming, at least more than ten times that of FHED.

C. Extension to Touzi Decomposition

Since both FHED and scattering vector model proposed by Touzi *et al.* [5], [6] are based on the Kennaugh–Huynen condiagnolization, a comparison is made in this subsection and the method of deriving the analytical solution is also extended to the Touzi decomposition.

The definitions of POA ψ and helicity angle τ of the two algorithms are the same, and the scattering matrix $[S]$ of a single target will be diagonalized after deorientation and dehelicity operations. The difference between FHED and Touzi decomposition comes from their different parameterization of the diagonalized scattering matrix $[S]$, where the former uses parameters γ_n and ν, and the latter uses complex-scattering-type parameters α_s (magnitude) and Φ_{α_s} (phase). Concretely, FHED has

$$\frac{S_{\mathrm{VV}}}{S_{\mathrm{HH}}} = \tan\gamma_n e^{-j4\nu} \tag{43}$$

and Touzi decomposition has

$$\frac{S_{\mathrm{HH}} - S_{\mathrm{VV}}}{S_{\mathrm{HH}} + S_{\mathrm{VV}}} = \tan\alpha_s e^{j\Phi_{\alpha_s}} \tag{44}$$

where $\alpha_s \in [0^\circ, 90^\circ]$ and $\Phi_{\alpha_s} \in [-90^\circ, 90^\circ]$. The information that (43) and (44) exploit is the same essentially, while the two have different "preferences" in capturing the target characteristics. As aforementioned, γ_n and ν_n is related to the target polarization sensitivity and the number of bounces of the reflected signal, respectively. On the other hand, α_s and Φ_{α_s} are interpreted as parameters indicating the scattering mechanism and relative phase, which have been successfully applied to wetland classification [5], [6].

Note that similar to FHED, α_s and Φ_{α_s} of a single target can also be solved analytically and represented by Huynen parameters, as

$$\alpha_s = \tan^{-1}\left(\sqrt{\frac{B_0\left(H^2+C^2\right) - A_0F^2}{A_0\left(H^2+C^2+F^2\right)}}\right) \tag{45}$$

$$\Phi_{\alpha_s} = \tan^{-1}\left(\frac{CD-HG}{H^2+C^2}\right). \tag{46}$$

The used Huynen parameters and their representations are very similar to (33) and (34). It can be inferred that, compared with Φ_{α_s}, α_s is more relevant to the target scattering mechanism, which plays a similar role like ν_n. For instance, for the ideal surface scattering, both α_s and ν_n take their minimum value 0, and for the double-bounced scattering, both α_s and ν_n take the maximum value, i.e., $\alpha_s = 90^\circ$ and $\nu_n = 45^\circ$. Actually, for the temporal PolSAR data employed in this article, ν_n extracted by FHED shows high consistency with symmetric scattering type magnitude α_{s1}, the subscript "1" of which means that it is extracted from the principal eigenvector of the coherency matrix $[T]$. Their correlation coefficients are 0.8311, 0.8205, and 0.8087, respectively, indicating that the two have similar physical significance of the target. Nevertheless, it still needs further efforts to explore whether the analytical solution of the Touzi decomposition can be applied to distributed target directly and how it will behave differently from the original parameters, which will be the next step of our research.

VI. CONCLUSION

This article proposes a FHED approach in order to computing H–E parameters with high efficiency. Besides, by analyzing the compressed range and ambiguity problem of the original H–E decomposition, new polarizability angle and new skip angle are proposed to improve the target recognition ability. Experimental results on temporal PolSAR data of disaster-affected area indicate that the degree of damage does not seem to have a specific effect on the new polarizability angle, while the new skip angle can be regarded as an index of the building DL, and its building damage mapping shows nice consistence with the results obtained by the widely used MBD. In terms of the time consumption for extracting parameters, FHED by solving analytical solutions of H–E parameters outperforms UT, ED, and even MBD, which leads to its undoubted superiority in rapid response to disasters. Besides, the relationship between FHED and Touzi decomposition is also discussed, as well as the analytical solution of Touzi parameters. The high coherence between the new skip angle and the symmetric scattering type magnitude also confirms the efficacy of the proposed in target characteristic description. Therefore, there is a good prospect of FHED in disaster monitoring and damage assessment.

ACKNOWLEDGMENT

The authors would like to thank the Japan Aerospace Exploration Agency (JAXA) for providing the outstanding ALOS-PALSAR polarimetric SAR data. The authors would also like to thank the anonymous reviewers for their pertinent comments and constructive suggestions in making this article a better presentation.

REFERENCES

[1] J.-S. Lee and E. Pottier, *Polarimetric Radar Imaging: From Basics to Applications*. Boca Raton, FL, USA: CRC Press, 2009.
[2] J. R. Huynen, "Phenomenological theory of radar targets," Ph.D. dissertation, *Dept. Elect. Eng., Math. Comput. Sci., Tech. Univ. Delft*, Delft, The Netherlands, 1970.
[3] W. L. Cameron, N. N. Youssef, and L. K. Leung, "Simulated polarimetric signatures of primitive geometrical shapes," *IEEE Trans. Geosci. Remote Sens.*, vol. 34, no. 3, pp. 793–803, May 1996.
[4] W. L. Cameron and H. Rais, "Derivation of a signed Cameron decomposition asymmetry parameter and relationship of Cameron to Huynen decomposition parameters," *IEEE Trans. Geosci. Remote Sens.*, vol. 49, no. 5, pp. 1677–1688, May 2011.
[5] R. Touzi, "Target scattering decomposition in terms of roll-invariant target parameters," *IEEE Trans. Geosci. Remote Sens.*, vol. 45, no. 1, pp. 73–84, Jan. 2017.
[6] R. Touzi, A. Deschamps, and G. Rother, "Phase of target scattering for wetland characterization using polarimetric C-band SAR," *IEEE Trans. Geosci. Remote Sens.*, vol. 47, no. 9, pp. 3241–3261, Sep. 2009.
[7] Y. Yamaguchi, A. Sato, W.-M. Boerner, R. Sato, and H. Yamada, "Four-component scattering power decomposition with rotation of coherency matrix," *IEEE Trans. Geosci. Remote Sens.*, vol. 49, no. 6, pp. 2251–2258, Jun. 2011.
[8] L. Liang, Y. Zhang, and D. Li, "A novel method for polarization orientation angle estimation over steep terrain and comparison of deorientation algorithms," *IEEE Trans. Geosci. Remote Sens.*, to be published, doi: 10.1109/TGRS.2020.3013203.
[9] F. Zhu, Y. Zhang, and D. Li, "A novel deorientation method in PolSAR data processing," *Remote Sens. Lett.*, vol. 7, no. 11, pp. 1083–1092, Aug. 2016.
[10] T. Dallmann and D. Heberling, "Technique for Huynen-Euler decomposition," *Electron. Lett.*, vol. 53, no. 13, pp. 877–879, 2017.
[11] C. Baird, W. T. Kersey, R. Giles, and W. Nixon, "Classification of targets using optimized ISAR Euler imagery," in *Proc. Radar Sensor Technol. X*, vol. 6210. Int. Soc. Opt. Photon., 2006, Art. no. 62100A.
[12] G. Singh, Y. Yamaguchi, W.-M. Boerner, and S.-E. Park, "Monitoring of the March 11, 2011, off-Tohoku 9.0 earthquake with super-tsunami disaster by implementing fully polarimetric high-resolution POLSAR techniques," *Proc. IEEE Proc. IRE*, vol. 101, no. 3, pp. 831–846, Mar. 2013.
[13] M. Sato, S.-W. Chen, and M. Satake, "Polarimetric SAR analysis of tsunami damage following the March 11, 2011 East Japan earthquake," *Proc. IEEE Proc. IRE*, vol. 100, no. 10, pp. 2861–2875, Oct. 2012.
[14] S.-W. Chen, X.-S. Wang, and M. Sato, "Urban damage level mapping based on scattering mechanism investigation using fully polarimetric SAR data for the 3.11 East Japan earthquake," *IEEE Trans. Geosci. Remote Sens.*, vol. 54, no. 12, pp. 6919–6929, Dec. 2016.
[15] Y. Yamaguchi, "Disaster monitoring by fully polarimetric SAR data acquired with ALOS-PALSAR," *Proc. IEEE*, vol. 100, no. 10, pp. 2851–2860, Oct. 2012.
[16] D. Li, Y. Zhang, L. Liang, J. Yang, and X. Wang, "Monitoring of tsunami/eaqthquake damages by polarimetric microwave remote sensing technique," in *Tsunami—Damage Assessment Medical Triage* (ISBN: 978-953-307-431-3). IntechOpen, 2020.
[17] Y. Lou, D. Clark, P. Marks, R. J. Muellerschoen, and C. C. Wang, "Onboard radar processor development for rapid response to natural hazards," *IEEE J. Sel. Top. Appl. Earth Obs. Remote Sens.*, vol. 9, no. 6, pp. 2770–2776, Jun. 2016.
[18] D. Li and Y. Zhang, "Random similarity-based entropy/alpha classification of PolSAR data," *IEEE J. Sel. Top. Appl. Earth Obs. Remote Sens.*, vol. 10, no. 12, pp. 5712–5723, Dec. 2017.
[19] D. Li and Y. Zhang, "Unified Huynen phenomenological decomposition of radar targets and its classification applications," *IEEE Trans. Geosci. Remote Sens.*, vol. 54, no. 2, pp. 723–743, Feb. 2016.
[20] C. Baird, W. Kersey, R. Giles, and W. Nixon, "Exploitation of ISAR imagery in Euler parameter space," in *Proc. Radar Sensor Technol. IX*, vol. 5788. Int. Soc. Opt. Photon., 2005, pp. 116–127.
[21] T. Dallmann and D. Heberling, "On the coneigenvalue decomposition of sinclair matrices," in *Proc. Prog. Electromagnetics Res. Symp.*, 2015, pp. 258–262.
[22] Wikipedia, "2011 Tōhoku Earthquake and Tsunami." [Online], Available, https://en.wikipedia.org/wiki/2011_T%C5%8Dhoku_earthquake_and_tsunami.
[23] S. R. Cloude and E. Pottier, "An entropy based classification scheme for land applications of polarimetric SAR," *IEEE Trans. Geosci. Remote Sens.*, vol. 35, no. 1, pp. 68–78, Jan. 1997.
[24] S.-W. Chen, X.-S. Wang, and S.-P. Xiao, "Urban damage level mapping based on co-polarization coherence pattern using multitemporal polarimetric SAR data," *IEEE J. Sel. Top. Appl. Earth Obs. Remote Sens.*, vol. 11, no. 8, pp. 2657–2667, Aug. 2018.
[25] S. Liu *et al.*, "Building damage mapping based on Touzi decomposition using quad-polarimetric ALOS PALSAR data," *Front. Earth Sci.*, pp. 1–12, 2020.

Liting Liang (Student Member, IEEE) received the B.S. degree in electronic information engineering from the Harbin Engineering University, Harbin, China, in 2016. She is currently working toward the Ph.D. degree in electromagnetic and microwave technology with the National Space Science Center, Chinese Academy of Sciences, Beijing, China.

Her research interest includes polarimetric synthetic aperture radar image processing and classification.

Yunhua Zhang (Member, IEEE) received the B.S. degree in electrical engineering from Xidian University, Xi'an, China, in 1989 and the M.S. and Ph.D. degrees in electrical engineering from Zhejiang University, Hangzhou, China, in 1993 and 1995, respectively.

He is currently a Professor with the National Space Science Center, Chinese Academy of Sciences, Beijing, China, and the Director of the CAS Key Laboratory of Microwave Remote Sensing. He is also a Professor with the School of Electronic, Electrical and Communication Engineering, University of Chinese Academy of Sciences, Beijing, where he lectured modern radar theory and technology to the postgraduate students. His research interests include the system design and signal processing of microwave sensors (high-resolution radar, interferometric radar, radar altimeter, and noise radar), polarimetric radar target decomposition, application of compressive sensing in radar, and antennas and computational electromagnetics.

Dr. Zhang is the Chief Designer for the Chinese Tiangong-2 Interferometric Imaging Altimeter, which is the first spaceborne wide-swath radar altimeter launched in September 15, 2016.

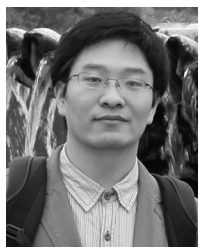

Dong Li (Member, IEEE) received the B.S. degree in electronic engineering from Xidian University, Xi'an, China, in 2008 and the Ph.D. degree in electrical engineering from the University of Chinese Academy of Sciences, Beijing, China, in 2013.

He is currently a Professor with the CAS Key Laboratory of Microwave Remote Sensing, National Space Science Center, Chinese Academy of Sciences, Beijing. His research interests include synthetic aperture radar (SAR) polarimetry, polarimetric target decomposition, polarimetric scattering modeling, SAR image registration, and computer SAR vision.

Dr. Li was elected as a Member of the Youth Innovation Promotion Association, Chinese Academy of Sciences in 2014. He was a recipient of the President Scholarship for Outstanding Students of Chinese Academy of Sciences in 2013 for his Ph.D. dissertation on the stereo processing and polarimetric analysis of SAR images.